Nano Today 62 (2025) 102697

Contents lists available at ScienceDirect

Nano Today

journal homepage: www.elsevier.com/locate/nanotoday

Photo-driven electronic skin enable activation of calcium channel for refractory wound healing

Jingjing Tian [a], Jiahao Li [b], Zhihong Wu [c,d,e], Lan Yin [f], Xing Sheng [g], Zhou Li [h], Hai Wang [b,*], Huachun Wang [i,*], Yu Zhao [b,j,k,**]

[a] Biomedical Engineering Facility of National Infrastructures for Translational Medicine, Peking Union Medical College Hospital, Chinese Academy of Medical Sciences and Peking Union Medical College, Beijing 100730, China
[b] Department of Orthopaedic Surgery, Peking Union Medical College Hospital, Chinese Academy of Medical Science and Peking Union Medical College, Beijing 100730, China
[c] State Key Laboratory of Complex Severe and Rare Diseases, Peking Union Medical College Hospital, Chinese Academy of Medical Sciences and Peking Union Medical College, Beijing 100730, China
[d] Beijing Key Laboratory for Genetic Research of Skeletal Deformity, Beijing 100730, China
[e] Key Laboratory of Big Data for Spinal Deformities, Chinese Academy of Medical Sciences, Beijing 100730, China
[f] The Key Laboratory of Advanced Materials of Ministry of Education, State Key Laboratory of New Ceramics and Fine Processing, School of Materials Science and Engineering, Tsinghua University, Beijing 100084, China
[g] Department of Electronic Engineering, Beijing National Research Center for Information Science and Technology, Center for Flexible Electronics Technology, IDG/McGovern Institute for Brain Research, Tsinghua University, Beijing 100084, China
[h] Beijing Key Laboratory of Micro-nano Energy and Sensor, Beijing Institute of Nanoenergy and Nanosystems, Chinese Academy of Sciences, Beijing 101400, China
[i] School of Integrated Circuits, Shenzhen Campus of Sun Yat-sen University, Shenzhen 518107, China
[j] State Key Laboratory of Common Mechanism Research for Major Diseases, Beijing 100005, China
[k] Institute of Basic Medical Sciences, Chinese Academy of Medical Sciences and Peking Union Medical College, Beijing 100005, China

ARTICLE INFO

Keywords:
Diabetic
Electronic skin
Fibroblasts
Photo-driven
Wound healing

ABSTRACT

The growing threat of refractory wound has created imperative need for the exploration of novel repair materials and therapeutic strategies. The disrupted endogenous electric fields in refractory wound may prolong the healing process. Hence, apply exogenous electrical stimulation to reestablish endogenous electric fields may be a promising way for refractory wounds treatment. Herein, a photo-driven electronic skin consist of p-type Si thin-film and near-infrared light was developed. This electronic skin could electrically modulate the intracellular calcium oscillation and significantly promote the fibroblasts' adhesion, proliferation and migration. Specifically, the average spreading area achieved 1.23 times higher than plane group after 24 h seeding. The cell proliferation quantity was 117 % higher than plane group after 3 days' PES treatment. As for cell migration, the complete wound closure was observed at 48 h in all the PES treatment group compared to 76.47 ± 1.23 coverage area in control group. Furthermore, it demonstrated rapid closure rate of a full-thickness circular diabetic skin defects with photoelectric stimulation (PES) derived from electronic skin, the wound was almost healed at 14 days' treatment. Furthermore, the expression level of pro-inflammation factors of IL-1β and TNF-α were reduced. Proteomic analysis showed that the metabolism process, the cellular processes of transport and catabolism, cell motility were remarkably promoted after PES treatment. The transport and catabolism process may regulate by mTOR signal pathway, and the increased cellular processes of cell motility may result of actomyosin contractility. This photo-driven electronic skin not only provided a facile therapeutic strategy and theoretical basis for refractory wound, but also provided a novel insight into potential mechanism underlying electrical stimulation promoting tissue repair.

* Corresponding authors.
** Corresponding author at: Department of Orthopaedic Surgery, Peking Union Medical College Hospital, Chinese Academy of Medical Science and Peking Union Medical College, Beijing 100730, China.
E-mail addresses: wanghai907@hotmail.com (H. Wang), wanghch36@mail.sysu.edu.cn (H. Wang), zhaoyupumch@163.com (Y. Zhao).

https://doi.org/10.1016/j.nantod.2025.102697
Received 22 October 2024; Received in revised form 17 February 2025; Accepted 24 February 2025

Introduction

Refractory wound such as chronic and non-healing wound seriously impact the human health and health care system due to the increasing prevalence and cost. More than 8.2 million people was affected by chronic and non-healing wounds, resulting in $28.1 to $ 96.8 billion medicare cost for all wounds, among which diabetic and surgical wounds were the most expensive to treat [1]. In case of chronic or non-healing wound, the healing process gets severely obstructed due to the pathophysiological conditions [2]. The primary objective for wound treatment is to achieve rapid wound closure and improve the healing process. There were numbers of strategies have proposed and evolved to treat chronic or non-healing wound [3], such as surgical debridement, offloading and removal of nonviable wound tissue [4,5], bandages [6], wound dressings [7,8], ultrasound [9], and negative-pressure wound therapy [10]. However, these treatments are only moderately effective, since they are passive and do not actively respond or regulated to variations in the wound environment [11]. Recently, growth factors or stem cell [12] mediated strategies were proposed as effective way to promote wound healing. But the rapid degradation, the bioactivity losing and the reversible differentiation of stem cell are the challenges and limited their clinical application [13,14]. Besides, Metal-organic frame materials (MOFs) and MOF-based transdermal drug delivery systems also shown enormous potential in refractory wound healing due to its unique performance in inhibit inflammation, enhance collagen deposition angiogenesis, and induce proliferation [15,16]. Compared with those biochemical therapies, biophysical manners have the advantages of high spatial and temporal resolutions, more stable and tunable when interacting with biosystems [17–20]. Furthermore, it was found that the skin wound has an endogenous electric field [21,22], which provoking the external electric stimulation used for accelerating wound healing process of chronic or non-healing wounds.

Electrical stimulation in wound treatment was first observed and researched in 1960s [23], which speeded wound healing process by increasing capillary density and perfusion, improving wound oxygenation, encouraging granulation and fibroblast activity [24–26]. Traditional electrical treatment regimens including direct current, pulsed current and alternating current, which need electrode, external power devices and electrode wire to connect [27–29]. Those types of electrical stimulation may pose constrains such as the increased size, the risk of infection and the displacement of electrode [27]. Therefore, the safety and longevity of the active stimulation system still face huge challenge. Besides, all the above units of stimulation systems should be portable, implantable and degradable for the clinical use, hence a simple and convenient electrical stimulation scaffold was urgently need and has great prospect in clinical application.

Recently, electrically active materials and scaffolds have arisen considerable attentions that can electrical stimulate the damaged tissue wirelessly [30–32] or self-powered [33,34], and have the advantages of miniaturization and integration [35]. Among all the proposed electrically active materials, Si-based scaffold could serve as the desirable photo-driven scaffolds for regenerative medicine due to their excellent biodegradability and biocompatibility [36]. Si-based scaffold displays many size-dependent properties, for examples, Si nanowires can be internalized into cells and forming active interfaces with intracellular cytoskeletal systems [37,38]. Si membrane structures could build tight extracellular interfaces with single cell or small tissues by protein-associated tethering, active motions, and dynamic cellular focal adhesions [38]. Si mesh scaffolds could create a conformal interface with soft organ such as brain cortex [39]. However, simple plane p-type Si film-based scaffold can be not served as electrically active scaffolds since its photoresponse components are small, Merrill et al. have proposed a Au-coated p-i-n Si multilayered membrane to acquire the strongest electrical stimulation for *in vivo* studies [40], wang et al. employed p-type Si film with micro-pillar to realize photoelectric stimulation for cranial defects repair [41]. In addition, it has demonstrated that the Si membranes based photo-driven scaffolds can significantly promote the proliferation and production of neurotrophic factors in schwann cells [42], and could modulate the membrane potentials and intracellular calcium dynamics of mesenchymal stem cells and then potentiate cell proliferation and differentiation [41]. However, the interplay between optical/electrical signals derived from Si film-based scaffold and fibroblast during the skin regeneration process has not exploited yet.

In this study, a Si-based photo-driven electronic skin for refractory wound healing was proposed. This electronic skin was composed of p-type Si thin-film with micro-pillar structure to convert the optical signal into electrical signal and enhance the conduction of endogenous electric filed. Compared with other photo-driven scaffold, this Si thin-film has the advantage of biocompatibility, biodegradable and high stability. And the degradation product is biocompatible, resorbable, and naturally present in human body [43]. In the other hand, environmental pollution especially water sources by drug compounds is a major problem for life bodies [44,45], whereas, this photo-driven electronic skin we used for wound heling avoided the use of drugs, hence the critically aquatic environment pollution caused by the common drugs could greatly reduce or avoid.

Furthermore, the micro-pillar structures also provided a favorable topographical support for the adhesion and growth of cells. With photoelectric stimulation (PES) derived from electronic skin, the electrical signals could evoke the calcium influx and actomyosin contractility, leading to the promotion of cell proliferation and migration ability. In addition, accelerated diabetic wound healing process was achieved by the PES treatment in C57BL/6 mice, and the level of pro-inflammation factors of IL-1β and TNF-α were down-regulated, suggesting the improved therapeutic efficacy with PES treatment *in vivo*. These results were further validated through proteomic analysis, which shows that the speeded wound healing process was associate with the promoted metabolism process. The increased cell proliferation was associated with the up-regulated cell process of transport and catabolism that mediated by mTOR signal pathway, and the elevated cell migration ability was related to the up-regulated cell motility mediated by actomyosin contractility and calcium influx. This work not only expanded the application of photo-driven Si thin-film scaffold on wound healing, but also offer a new therapeutic strategy and theoretical basis for refractory wound healing.

Results and discussion

Biophysical cues such as electrical, mechanical and topographical signals could influence or communicate with biological systems and then affect tissue repair progress. However, the precise tools for introduce localized physical stimulation and response to the biophysical signals with high spatiotemporal resolution are limited [46]. Therefore, photo-driven scaffold was proposed, photo-driven scaffolds mainly consist of light responsive materials, such as quantum dots, gold nanomaterials, transition-metal dichalcogenides, up-conversion nanoparticles, organic semiconductors, compound semiconductors and silicon semiconductors. Quantum dots (QDs) have unique optical properties of resistance to photobleaching and high/narrow light emission, but the cytotoxicity caused by the constituent materials ultimately precluded the FDA approval of QDs for further clinical applications [47]. Gold nanomaterials possess particularly advantages of robust synthesis methods, high yield and not require further phase transfer to water. However, the toxicological property about the induction of oxidative stress and genotoxicity can't be ignored [48]. Organic semiconductors such as carbon nanomaterials of carbon nanotubes (CNTs), graphene, carbon dots and nanodiamonds have widely investigated for various applications due to their distinct electrical, magnetic, optical mechanical and chemical properties. However, the critical safety issue is still controversial with conflicting opinions [49]. Transition-metal dichalcogenide, up-conversion nanoparticles and compound

semiconductors have the drawbacks of toxicity, biostability and high cost, respectively [47].

Compared to other photo-driven scaffolds, silicon based scaffolds may not possess the highest photoelectric conversion efficiency, but they have the better biocompatibility and high stability. Moreover, the silicon scaffold is biodegradable through a hydrolysis process, and the degradation product is biocompatible, resorbable, and naturally present in human body [43]. In addition, Si-based semiconductor materials showed many relevant electrical and optical properties, and have been explored as many electronic and photonic devices. Si-based semiconductor materials could generate functional interfaces with biological systems ranging from proteins to organs derive from the photoelectric convertibility, which could convert a light signal into electrical or electrochemical outputs. Then exert photoelectric stimulation and modulate the concentration distribution of ions and/or change the biological response. Hence, a p-type Si scaffold was selected due to its outstanding localized PES performance and stability.

Herein, a photo-driven electronic skin composed of p-type Si thin-film with micro-pillar 3D structures and NIR irradiation unit was fabricated for refractory wound healing (Scheme 1). As shown in Fig. 1a, the p-type Si thin-film possesses a diameter of 1×10^{-6} m and a height of 2×10^{-6} m micro-pillar on the surface, which could generate pulsed electrical signals under NIR irradiation and furtherly modulate biological activities. The optoelectronic response performances of p-type Si thin-films in phosphate buffer saline (PBS) were systematically evaluated using the standard patch-clamp technique. Here, a glass pipette electrode was positioned onto the p-type Si thin-film to record photocurrents signals under an 808 nm laser irradiation (Fig. 1b). The optoelectronic response is primarily attributed to the build-in electric field established in the interface of p-type Si thin-film and PBS solution,

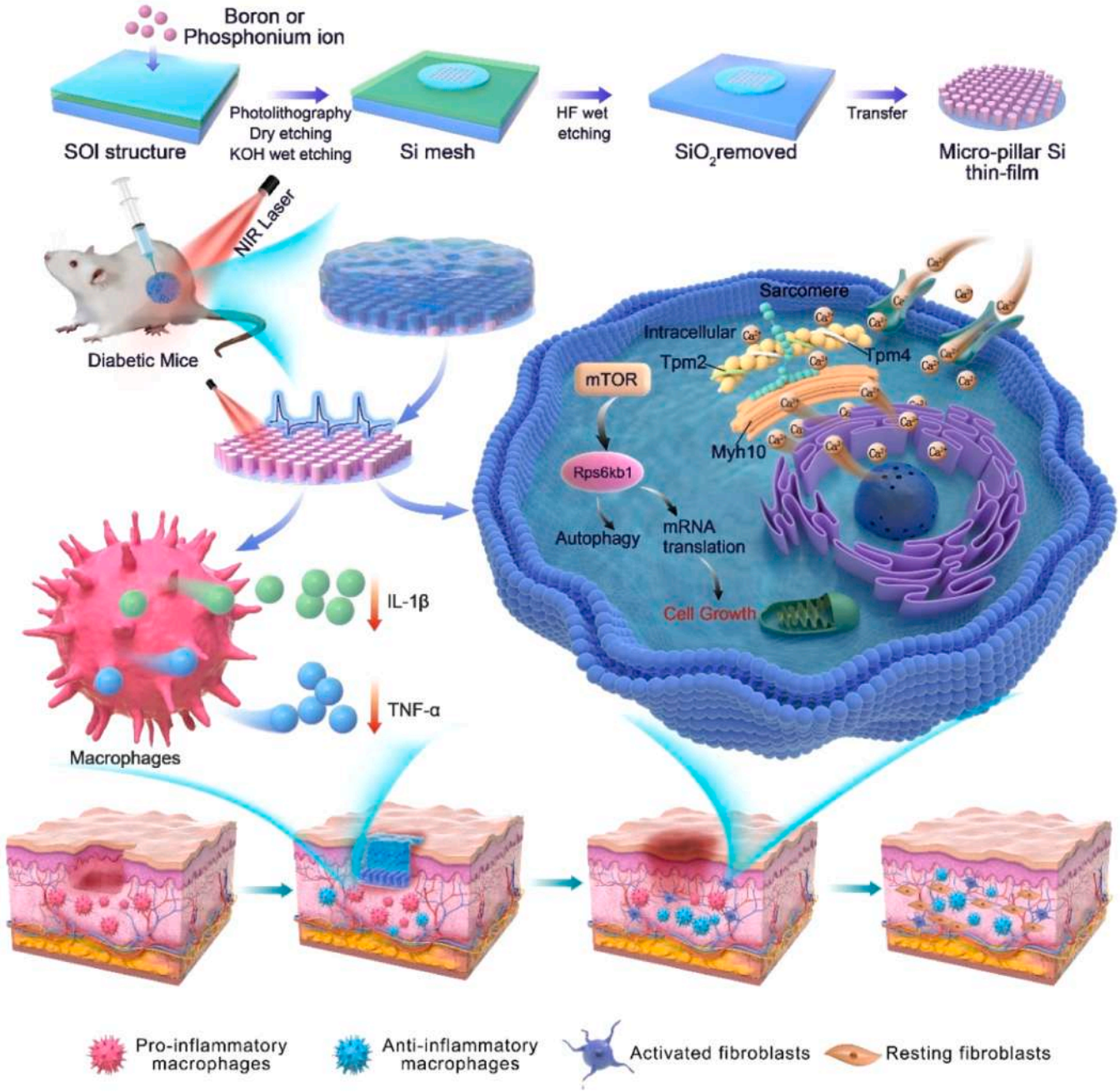

Scheme 1. Synthesis process of the Si-based photo-driven electronic skin and its application on diabetic wound healing.

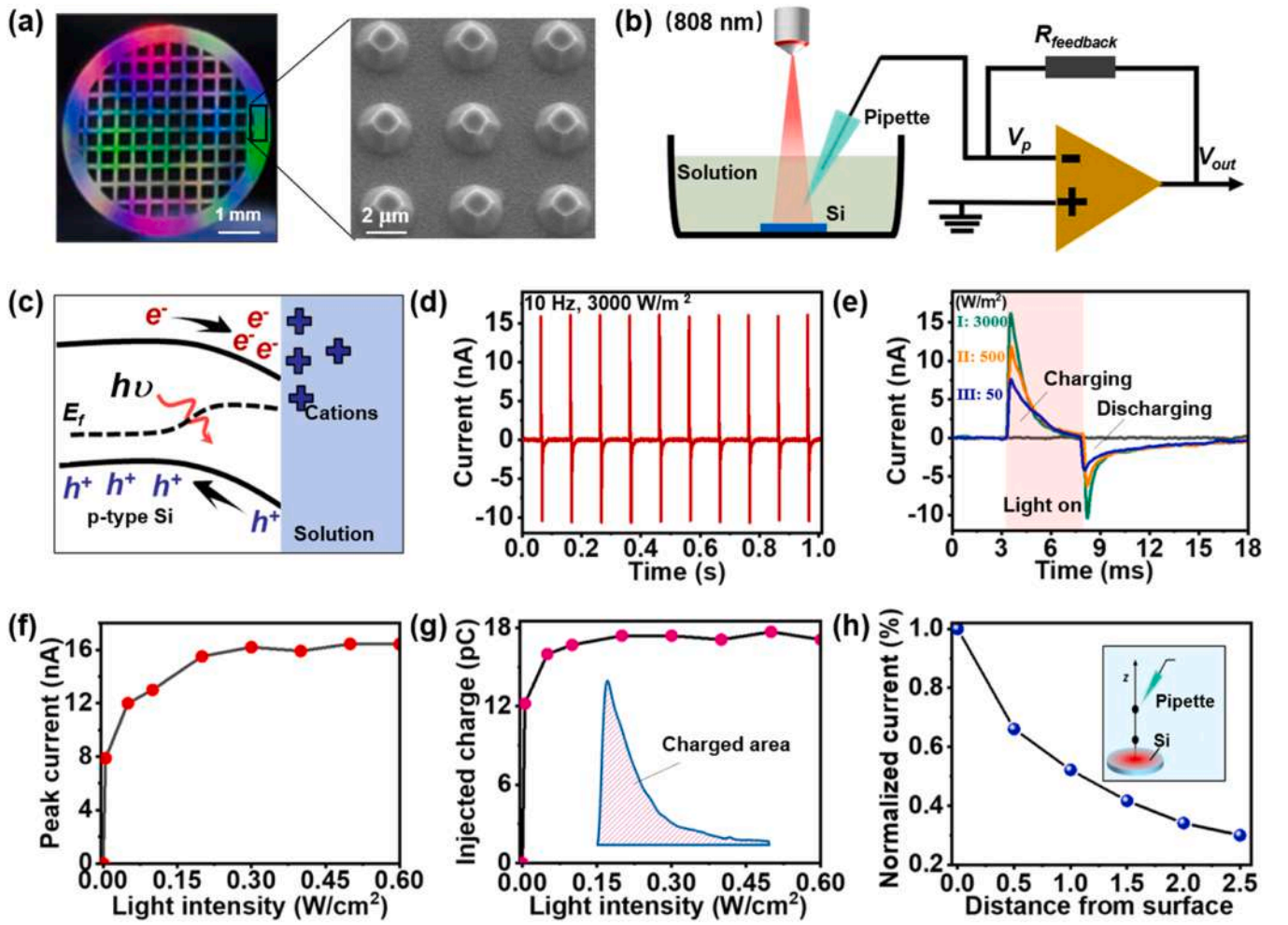

Fig. 1. The optoelectronic response of micro-pillar p-type Si thin-film. (a) Optical and SEM images of the p-type Si thin-film with micro-pillar 3D structures. (b) Scheme for the photocurrent measurement of p-type Si thin-film floating in the PBS solution. (c) Energy diagram illustrating the cations accumulation at the interface of p-type Si thin-film and PBS solution. (d) Photocurrent response curves of p-type Si thin-film under 808 nm laser irradiation, with the power density, pulse width and frequency were 0.3 W/cm^2, 5 ms and 10 Hz respectively. (e) Photocurrent responses of p-type Si thin-films under different intensities NIR irradiation, line I refers to 3000 W/m^2, line II refers to 500 W/m^2, and III refer to 50 W/m^2. Peak current (f) and injected charges (g) variation versus NIR intensity of p-type Si thin-film, respectively. (h) Measured photocurrent as a function of vertical distance z in PBS solution.

which effectively separates the photo-generated electrons and holes, leading to cations accumulation at the interface, as depicted in Fig. 1c. To enhance the separation efficiency of photogenerated charge carriers and subsequently improve the optoelectronic response of the device, the fabrication of nanostructures or heterojunctions is a promising approach. This is primarily due to the unique band structure of such configurations, which facilitates the effective separation of electrons and holes [50–52].Fig. 1d illustrated the photocurrent response collected from a floating p-type Si thin-film under the irradiation of pulsed NIR irradiation (10 Hz, 3000 W/m^2). The p-type Si thin-film responds fast to the NIR signals and exhibits the typical charging and discharging characteristics of a photocapacitor that can provide electrical pulse stimulation in biological aqueous environment. The higher irradiation intensities lead to the higher peak currents with larger charging area, demonstrating more cations accumulated at the interface of p-type Si thin-film and PBS solution (Fig. 1e). The photo-generated peak current and the amount of accumulated charges response at different NIR intensities were summarized in Figs. 1f and 1g. It is noted that they tend to be saturated when the irradiation intensity exceeds 1500 W/m^2.

In addition, the 3D spatial distribution of photocurrent signals was quantified by progressively varying vertical (z axis) distances between the pipette electrode and the illumination spot center on the surface of p-type Si thin-film (laser intensity 3000 W/m^2, spot size 4 mm). As demonstrated in Fig. 1h, the photocurrent gradually decreases with the increased distances z, which down to ~50 % of the maximum value at around z = 1 mm. These results indicate that the photoelectric modulation of p-type Si thin-film works within millimeter range, in our designed skin regeneration process the p-type Si thin-film is closely stick to skin and muscle tissue, which meanings the photocurrent could generate in skin and muscle tissue under NIR irradiation.

The microstructures on p-type Si thin-film could provide a spatial geometric configuration for various cell types' adhesion and activities [53,54]. Hence the cell activity regulation of micro-pillar p-type Si thin-film on fibroblast was investigated firstly, L929 was selected as model cell for detection. Firstly, the adhesion ability of L929 on p-type Si thin-film was evaluated, since cell adhesion is the first cell-material interaction and is fundamental for growth and determines subsequent cellular events such as the proliferation and differentiation. As shown in Fig. 2a-h, the spreading and actomyosin contractility of L929 was characterized by immunofluorescent (IF) staining after seeding for 24 h, the F-actin and nucleus were stained green and blue by FITC-phalloidin and DAPI, respectively. The IF staining images revealed that L929 were normally adhered on micro-pillar p-type Si thin-film without distortion and contraction, and the relative numbers of adhesion cells in micro-pillar group were higher than plane group, and there have significant difference between two group ($p < 0.05$, Fig. 2g). This may

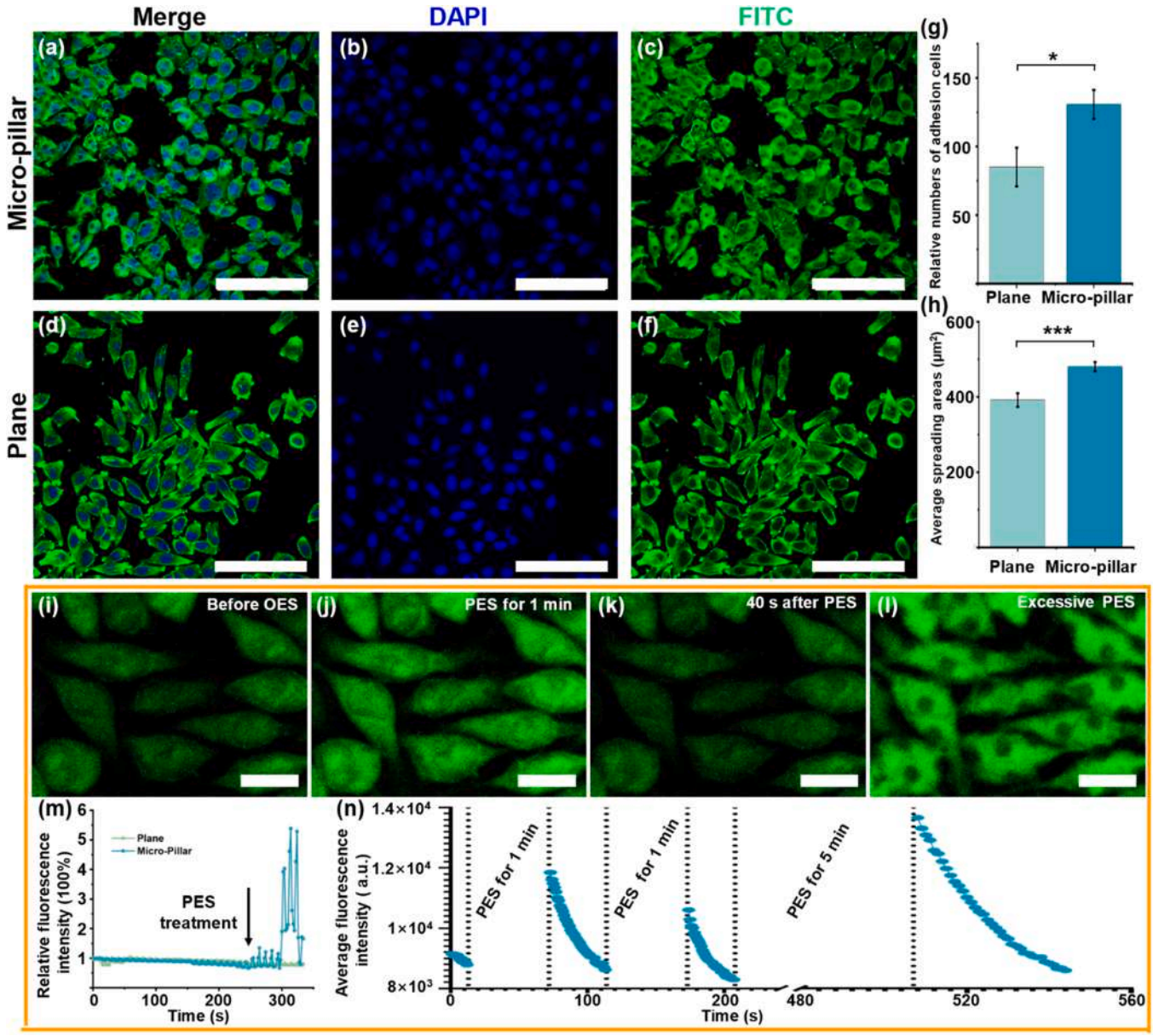

Fig. 2. The effects of micro-pillar p-type Si thin-film and its optoelectronic response on morphological and intracellular calcium ion level of L929 cells. The morphological images of L929 cultured on micro-pillar (a,b,c) and plane p-type Si thin-film (d,e,f) for 24 h, the F-actin was stained by FITC-phalloidin (green) and the nucleus were stained by DAPI (blue). Scale bar is 100 μm. (g) The relative numbers of adhesion cells on plane and micro-pillar p-type Si thin-film. (h) The average spearing areas of adhesion cells on plane and micro-pillar p-type Si thin-film (i-l) The intracellular calcium ion level of L929 cells influenced by PES derived from micro-pillar p-type Si thin-film. (m) The fluctuation of average fluorescence intensity on plane and micro-pillar p-type Si thin-film with NIR irradiation, triangle dots refer to plane and circle dots refer to micro-pillar (p-type Si thin-film). (n) The fluctuation of average fluorescence intensity shows intracellular calcium ion level of L929 cells after PES treatment for certain time. Scale bar is 20 μm. The two-tailed *t*-test was used for the statistical analysis.

cause by the enhanced adhesion force provided by micro-pillar.

In addition, the average spreading areas in two groups also have significant difference ($p < 0.001$, Fig. 2h), with the average spreading areas in micro-pillar group were about 1.23 times higher than plane group. Hence, we can conclude that more denser cell adhesion and thicker F-actin cables were established on micro-pillar p-type Si thin-film compared to plane Si membrane. These results indicate that L929 on micro-pillar p-type Si thin-film grew as normal as plane Si membrane, and the micro-pillar structures have certain positive effects on cell adhesion and actomyosin contractility [55]. The increased average spreading area may be caused by the adequate spaces between the neighboring micro-pillar [56]. The space between neighboring micro-pillar is 5 μm, which is equivalent and higher than the pseudopodium of cells. Therefore, fibroblasts can easily spread on or across the spaces between neighboring micro-pillar, thereby having positive influence on the adhesion and spreading of cells.

Afterwards, others cellular behaviors such as intracellular calcium oscillation dynamics, cell migration and proliferation activities affected by PES were further addressed. As we known that endogenous electrical signal participate in many essential biological process including embryonic development [57], differentiation of stem cell [41] and human memory [58], and influence various kinds of ionic passing back and forth through cell membranes [57]. Calcium channels is pivotal for fibroblast and play a key role in regulating cell function such as proliferation and migration [59], hence the dynamic change of intracellular calcium ion level influenced by PES derived from micro-pillar p-type Si thin-film was examined by live-cell imaging. As shown in Fig. 2i-l, calcium ion positive cells were dyed by Fluo-4 AM, and the real time

fluorescence intensity of intracellular Fluo-4 AM was imaged and recorded. After PES for 1 min (Fig. 2j,n), the mean fluorescence intensity was increased from 2.94 × 10^4 to 3.69 × 10^4, and the intensity value was decreased to 2.88 × 10^4 after the PES withdraw for 40 s (Fig. 2k), which is comparable to the value before PES treatment. When the PES time prolong to 5 min, the mean fluorescence intensity was increased to 3.94 × 10^4, which is slightly high than 1 min stimulation. It demonstrated that the fluorescence intensity will not rise indefinitely with the extension of time, and the NIR intensity density of 0.3 W/cm^2 have no adverse effects on fibroblast. However, when the light intensity density of NIR laser increased to 1 W/cm^2, the fluorescence intensity increased greatly and the cells were died since the cell borders beginning to blur (Fig. 2l).

To eliminate the influence of NIR on the fluctuation of average fluorescence intensity, the average fluorescence intensity on plane thin-film and micro-pillar p-type Si thin-film were monitored as shown in Fig. 2m. When the NIR irradiation was carried on 240 s, the average fluorescence intensity of intracellular calcium ion was increased drastically in micro-pillar p-type Si thin-film group, however, it was unchanged in plane p-type Si thin-film group with the NIR irradiation. This demonstrated that micro-pillar p-type Si thin-film are more conducive to activating calcium ion activity, since the calcium ion fluorescence intensity in plane p-type Si thin-film group remains almost unchanged even under a higher illumination intensity of 1 W/cm^2 (Fig S1). Therefore, those results provide solid evidence for that PES could modulate cytosolic calcium ion level, as we known that calcium ions and calcium ion channels play a vital role in cell behaviors regulation [60]. Hence this micro-pillar p-type Si thin-film based electronic skin that we fabricated offering an effective opportunity to regulate fibroblast behaviors such as the level of calcium ions and the regulation of calcium ion channels in a long and controllable manner.

As it demonstrated that PES could increase intercellular calcium ion level, then the fibroblasts' behaviors of migration and proliferation affected by PES were evaluated afterwards. The migration and proliferation ability of fibroblasts after PES treated for various time were observed by transwell and CCK-8 assays, respectively. The optimal PES treatment time was investigated firstly as shown in Fig. 3a-d, the amounts of transmembrane cells in transwell assay were imaged and counted after PES for 10, 20 and 30 min immediately, the transmembrane cells on p-type Si thin-film were stained by DAPI. The testing results showed that the transmembrane cells in all the PES treated groups were higher than control group (without stimulation) and have statistic difference (Fig. 3q), and the amount of transmembrane cells in 20 min PES treatment group was higher than 10 and 30 min group. Therefore, the PES treatment time of 20 min might be a more efficient way for fibroblast behaviors modulation and wound healing promotion.

Migration is a main phase in wound healing process and play a vital role in wound contraction and later healing, which begins several hours after injury [61]. Hence the migration ability of L929 fibroblast was further investigated by cell scratch assay *in vitro* to explore the critical mechanisms of action involved in the wound healing process. L929 was seeded on micro-pillar p-type Si thin-film and incubated in an 37℃ incubator until cell confluence, then a scratch was made by a 200 μL pipette tip on the monolayer of cells (Fig. 3e-h). After that, L929 was treated by PES for 10, 20 and 30 min, respectively. Then L929 was imaged and the wound closure area were calculated after cultured for 12, 24, 36 and 48 h as shown in Fig. 3e-p. The fastest wound healing rate was observed in the 20 min PES treatment group, and all stimulation groups were migrated significantly faster than control group. Briefly, the wound showed 24.81 ± 1.20, 41.71 ± 0.84, 39.02 ± 2.36 closure of the initial wound area in the 10, 20 and 30 min PES treatment group compared to 16.31 ± 1.31 in untreated group after 12 h incubation ($p < 0.01$, $p < 0.001$ and $p < 0.01$, Fig. 3e-l, s). And the wound closure values were increased to 54.60 ± 6.83, 72.22 ± 3.49, 54.70 ± 0.11 in 10, 20 and 30 min PES treatment group, and 32.94 ± 1.96 in control group after 24 h incubation ($p < 0.05$, $p < 0.001$ and $p < 0.001$, Fig3 e-h, m-p,

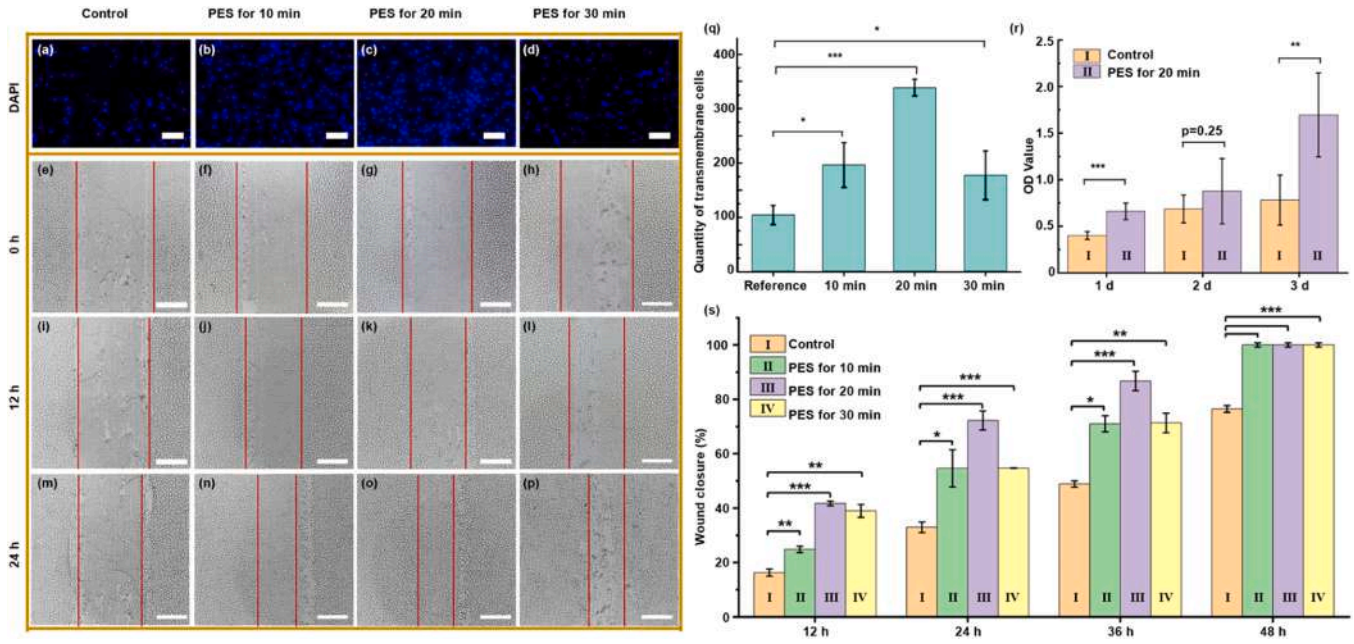

Fig. 3. The migration and proliferation ability of fibroblasts L929 cells with PES treatment. The transwell assay of L929 cells before (a) and after PES treatment for 10 min (b), 20 min (c) and 30 min (d), respectively. The nucleus was stained by DAPI (blue). (e,i,m) The migration of L929 cells in control group after scratched for 0, 12 and 24 h, respectively. (f,j,n) The migration of L929 in PES for 10 min group after scratched for 0, 12 and 24 h, respectively. (g,k,o) The migration of L929 in PES for 20 min group after scratched for 0, 12 and 24 h, respectively. (h,l,p) The migration of L929 in PES for 30 min group after scratched for 0, 12 and 24 h, respectively. (q) Quantitative analysis of the transmembrane cells with PES treatment for 10, 20 and 30 min, five in parallel. (r) The proliferation ability of L929 cells with PES treatment for 20 min per day evaluated by CCK-8 assay, six in parallel, line I refers to control group, line II refers to PES for 20 min group. (s) Quantitative analysis of the wound closure ratio at 12, 24, 36 and 48 h after PES treated for 10 min, 20 min and 30 min, respectively. line I II, III, IV refer to control group, PES for 10, 20, 30 min group, respectively. Three in parallel *$p < 0.05$, * *$p < 0.01$, * **$p < 0.001$. Scale bar is 200 μm. The two-tailed *t*-test was used for the statistical analysis.

s). Moreover, when the incubation time extended to 36 h, the wound area covered 70.99 ± 2.95, 86.74 ± 3.59, 71.33 ± 3.56 in 10, 20 and 30 min PES treatment group compared to 48.86 ± 1.15 in control group ($p < 0.05$, $p < 0.001$ and $p < 0.01$, Fig. 3s). The complete wound closure was observed at 48 h in all the PES treatment group compared to 76.47 ± 1.23 coverage area in control group ($p < 0.001$, Fig. 3s). Those results demonstrated that PES increased the migration rate of L929 fibroblasts significantly compared to non-treated group. As previous reported that the efficiency of the wound healing depends on the migration rate of the keratinocytes [62], and the non-migrating hyperproliferative keratinocytes are characteristic of non-healing diabetic wounds [63]. Therefore, the enhanced cell migration rate derived from PES treatment would be effective for refractory wound healing promotion.

Subsequently, cell proliferation influenced by PES was evaluated at 1, 2 and 3 d after seeding. CCK-8 assay was used to detect, after 10 μL CCK-8 added to per well, cells were placed into cell incubator for another 3 h to induce the formation of formazan, then the absorbance was read at 450 nm on a microplate reader. As shown in Fig. 3r, the cells in PES groups were increased statistically remarkably after stimulated for 1 and 3 d. There was no significant difference observed after PES treated for 2 d, but the increased quantity of proliferated cells was also found in PES group compared to control group. Specifically, the cells viability in PES group was 65 %, 27 % and 117 % higher than that of control group at 1, 2 and 3 d treatment, respectively. Those results indicated that PES derived from electronic skin could promote fibroblast cell proliferation significantly.

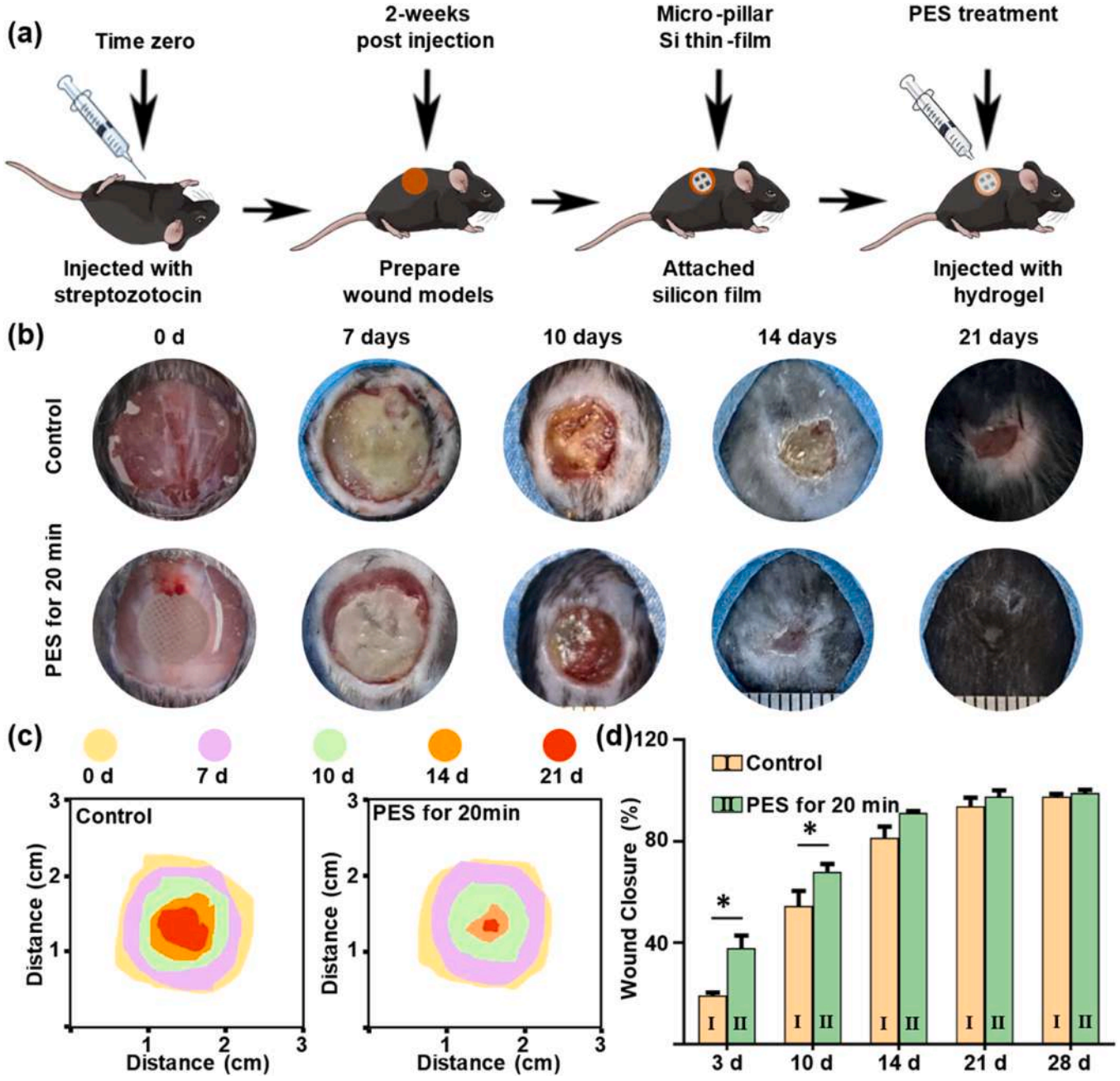

Fig. 4. The establishment of diabetic wound and the healing process with PES treatment. (a) Schematic diagram demonstrated the timeline of the operation process. (b) Photographs of the wound closure process with PES treatment at 0, 7, 10, 14 and 21 d post surgery. (c) Traces of wound closure area with PES treatment at 0, 7, 10, 14 and 21 d post surgery. (d) The statistical analysis of corresponding wound closure rates with PES treatment at 3, 10, 14, 21 and 28 d post surgery, line I refers to control group, line II refers to PES for 20 min group. *$p < 0.05$. The two-tailed *t*-test was used for the statistical analysis.

Diabetic foot ulcers (DFU) is a typical non-healing complication of diabetes and presents considerable challenges to the health care system, 15–25 % patients with diabetes will be affected by DFU [6], the annual cost for DFU wound management was 9–13 billion dollar in the United States [64]. However, the clinic treatment of DFU remains a challenge, the novel and effective wound dressing and repair means is still highly needed. Hence, to investigated whether the electronic skin that we fabricated could augment diabetic wound healing, a diabetic mice wound model was established, then the micro-pillar p-type Si thin-film and PES treatment were applied on it. The timeline of the operation process was schematic diagrammed in Fig. 4a, the diabetic mice model was established about two weeks after the injection of STZ, a full-thickness circle skin wound was made on the back of the C57BL/6 mice. Subsequently, the micro-pillar p-type Si thin-film was placed on the wound, and a thermosensitive hydrogel of chitosan/β-sodium glycerophosphate was injected on the wound to fix the micro-pillar p-type Si thin-film and avoid the microbial invasion simultaneously. The wound closure was recorded and calculated as shown in Fig. 4b-d, the wounds in PES group healed faster and well at days 3, 7, 10, 14, 21 and 28 post surgery, the wounds healing progress in control group was slowly and there is suppuration on the surface of wound. In brief, the wound closure rate in PES group was significantly faster than that of the control group, especially at 3 and 10 d after surgery ($p < 0.05$, Fig. 4d). Specifically, the wound healed rate in PES group were 42.42 ± 3.43 % and 65.23 ± 6.79 % compared to 18.44 ± 2.01 % and 50.41 ± 5.87 % at 3 and 10 d after surgery, respectively. Remarkably, there almost fully healed (only 8.37 % left) in PES group on day 14, and the wound was basically covered with newly formed skin tissue (Fig. 4b,c). These data showed that PES could speed up the healing rate of diabetic skin wound.

The diabetic mice wound model was established by streptozotocin (STZ) induction in this work, during which the blood glucose and weight level were monitored. As shown in Fig. 5a, the blood glucose level was increased from 8.8 to 24.57 mmol/L with the treatment of STZ, and the blood glucose level was maintained at a range of 8.5–9.77 mmol/L in control group, which is in the normal range of reference blood glucose level (4.44–11.1 mmol/L). The weight of mice was associatively

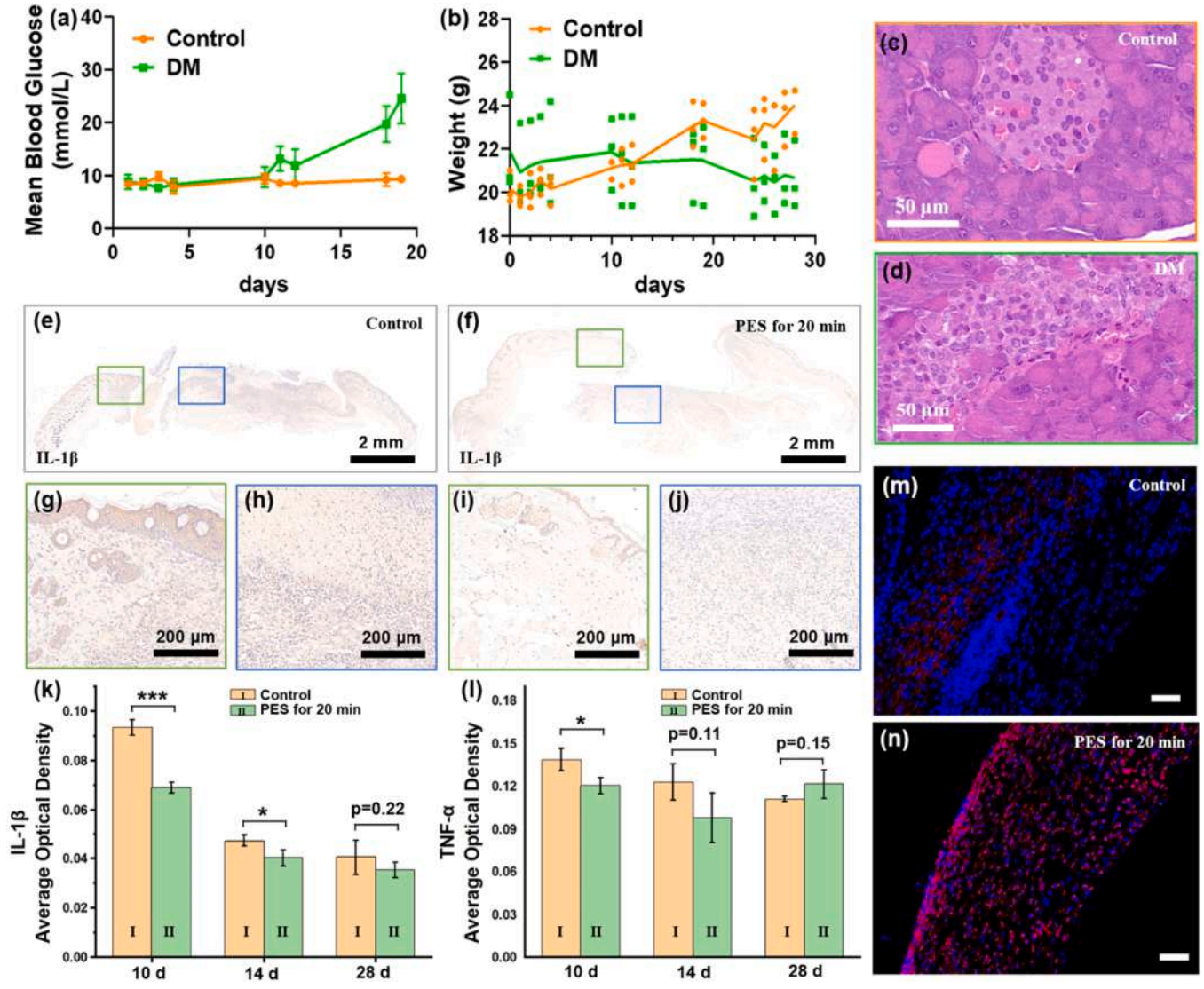

Fig. 5. The immunohistochemistry analysis of diabetic wound tissue with PES treatment. (a) The level of mean blood glucose fluctuation after STZ injection for various time. (b) The corresponding weight of the mice after STZ injection. Circle dots refer to control and square dots refer to DM group in (a) and (b). The H&E staining images showing the islet cell with (d) and without (c) STZ injection. Immunohistochemistry staining images of IL-1β in diabetic wound mice skin tissue with (f) and without (e) PES treatment at 10 d post surgery. The average optical density (AOD) values of IL-1β (k) and TNF-α (l) in diabetic wound mice skin tissue with PES treatment at 10, 14 and 28 d post surgery, line I refers to control group, line II refers to PES for 20 min group. Immunofluorescence staining image of p-MLC in diabetic wound mice skin tissue with (m) and without (n) PES treatment, the p-MLC was stained by cy3 (red) and the nucleus were stained by DAPI (blue), scale bar is 50 μm. *$p < 0.05$, * **$p < 0.001$. The two-tailed *t*-test was used for the statistical analysis.

decreased from 21.87 g to 20.67 g in the modeling process, however, the weight of mice without STZ injection was increased from 20.16 g to 24.03 g with the same feeding conditions (Fig. 5b). Therefore, the increased blood glucose level and the decreased weight illustrated the successful modeling of diabetic mice. Furthermore, the pancreas tissue of mice with and without STZ treatment was histomorphologically studied by haematoxylin and eosin (H&E) staining (Fig. 5c). The morphology of pancreas islet was changed from circular-like to indefinite shape, and the number of cells in pancreas islet was increased. Hence, not only the blood glucose level and weight were altered through the induction of STZ, but also the morphology or maybe the function of pancreas islet were changed, which will lead to metabolic disorders and slow or stall wound healing process.

Wound healing especially refractory wound healing is one of the most complex biological processes and including four overlapping distinct phases of hemostasis, inflammation, proliferation and remodelling [65]. Among which inflammation is recognized as the most dysregulated process of diabetic wound healing [66]. Diabetic wounds are characterized by a prolonged inflammatory phase and difficulty in healing due to the accumulation of pro-inflammatory macrophages and factors in the wound [67]. Hence, decreased pro-inflammatory microenvironment is benefit for diabetic wound healing. Therefore, the pro-inflammatory factor of interleukin-1 beta (IL-1β) and tumor necrosis factor-α (TNF-α) were selected to estimate the pro-inflammatory level after PES treatment. Immunohistochemistry (IHC) method was used to assess the expression proteins in diabetic wounding tissue after 10, 14 and 28 d post surgery. As shown in Fig. 5e-l, IL-1β and TNF-α were all showed suppressed expression in diabetic tissues after PES treatment compared to the control group. Particularly, IL-1β expression was significantly suppressed after 10 and 14 d's PES treatment ($p < 0.001$

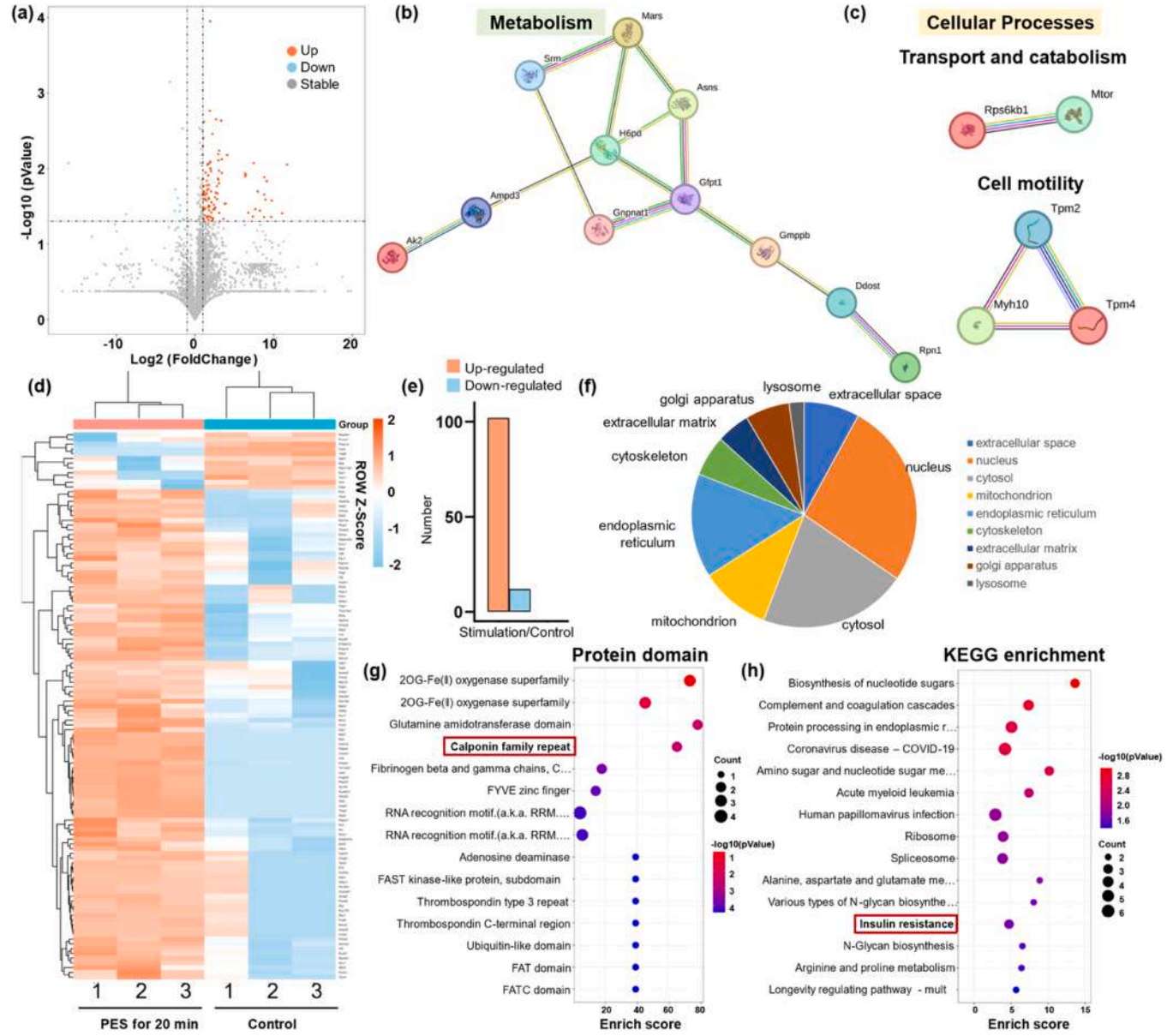

Fig. 6. Proteomics analysis of the differentially expressed proteins in diabetic wound tissue with PES treatment. (a) Volcano plot illustrated the fold change of protein expression with PES treatment group or not. (b) STRING analysis for significantly upregulated proteins in metabolism process. (c) STRING analysis for significantly upregulated proteins in cellular processes of transport and catabolism, cell motility. (d) Heatmap representation of the differentially expressed protein, the color scale represents the relative expression profiles. (e) The amount of differentially expressed proteins among two groups (orange: upregulated; blue: downregulated). (f) Subcellular localization classification showed the differentially expressed proteins were mainly concentrated in the nucleus and cytosol. (g) The result of protein domain enrichment analysis. (h) The result of KEGG enrichment analysis.

and $p < 0.05$), however, the IL-1β expression level has no significantly difference with control group at 28 d. Similarly, TNF-α was significantly suppressed after 10 d's PES treatment ($p < 0.05$), and there is no significantly difference was found with control group after 14 and 28 d's stimulation. These results demonstrated that PES treatment could suppress the expression of IL-1β and TNF-α in early inflammation phase, which may result of the suppressed pro-inflammatory macrophages expression in diabetic wound.

Diabetic patients or animal models have a pro-inflammatory baseline state before wounding, resulting in high level expression of pro-inflammatory cytokines [6]. The pathophysiologic alterations of diabetics blunt the wounded tissue to mount an acute inflammatory response to counteract injury and then impact the inflammation process of diabetic wound healing [68]. Hence, anti-inflammation or decreasing the pro-inflammation level will be the breakthrough for enhance diabetic wound healing. In addition, there have been proved that inhibition of the IL-1β expression could accelerate wound healing in diabetic mice [69]. While based the above results, we can conclude that PES treatment could decease the pro-inflammatory level through reduce the expression of IL-1β and TNF-α in inflammation phase, and then shorten the prolonged inflammatory period in chronic or non-healing wounds, thereby promoting the refractory wound healing process ultimately.

To further explore the underlying molecular mechanisms of PES treatment on diabetic wound healing, proteomic analysis was performed to detect the differentially expressed proteins. The criteria of $p < 0.05$ and fold change more than 2 were considered statistically significant (Fig. 6). Six samples of control and PES group ($n = 3$) showed the number of 3794 differentially expressed proteins. The heatmap illustrated that the up regulated proteins in PES group were closely related to metabolism and cellular process of transport and catabolism, cell motility, such as Ampd3, Ak2, mTOR, Tpm and Myh were all upregulated (Fig. 6a,d). As shown in volcano plot (Fig. 6a), 114 significantly differentially expressed proteins were identified, among which 102 proteins were upregulated (orange) and 12 proteins were downregulated (blue), the histogram was show in Fig. 6e. The protein interactions inferred from upregulated differentially expressed proteins by STRING were shown that cell metabolism processes such as purine, nucleotide, carbon and amino acid metabolism, and cell cellular processes such as transport and catabolism, cell motility were upregulated and activated (Fig. 6b,c). Furthermore, the activated transport and catabolism ability were associated with the mTOR signal pathway, since the increased expression of mTOR and Rps6kb1 can facilitate the mRNA translation level and promote cell growth (schematic 1). As for increased cell migration, it may result of the activated cell motility and actomyosin contractility.

To further verify this hypothesis, IF of p-MLC on skin tissue was carried out. As shown in Fig. 5m and n, PES treatment group exhibited higher expressions of p-MLC in diabetic mouse skin tissue. Combined with the former results of more cell adhesion was achieved under PES treatment, we can conclude that PES could active cellular contractility and migration ability. In addition, cell contractility was closely related to intracellular calcium ion level, and PES treatment could alter the level of intracellular calcium ion and calcium channel, hence the results defined *in vitro* were further verified our hypothesis. The pie charts (Fig. 6f) showed the subcellular localization of differentially expressed proteins, which were mainly located in the nucleus and cytosol (26.6 and 21.3 %), which also indicating that the differentially expressed proteins may related to the cellular processes. The protein domain enrichment analysis based on Pfam showed that PES group upregulated protein domains including calponin family repeat (Fig. 6g), which also confirmed the increased intracellular calcium ion. Kyoto Encyclopedia of Genomes (KEGG) enrichment analysis was used to detect all differentially expressed proteins. It revealed that those proteins were mainly enriched in the cellular and metabolic process (Fig. 6h), especially that the endocrine and metabolic disease of insulin resistance was enriched, which also confirmed the successful establishment of the diabetic mice model. Those results indicate that mTOR signal pathway and calcium ion voltage-gated channel may play an important role in PES promotion of wound healing, which were closely related to cell proliferation and motility, respectively.

Conclusion

In summary, we developed an environment friendly photo-driven electronic skin for refractory wound repair promotion, which composed of the micro-pillar p-type Si thin-film and an NIR irradiation unit. This electronic skin can convert the optical energy into a pulsed alternating current signal and exert the electrical stimulation directly on the wound to enhance skin regeneration of the refractory wound. It was demonstrated that the PES derived from electronic skin could arouse the elevation of intracellular calcium ion level through calcium ion voltage-gated channel, enhance the cell migration and proliferation ability of fibroblast *in vitro*. In addition, the promoted wound therapeutic effect was further demonstrated in diabetic mice, which showed a rapid closure rate of a full-thickness circle skin wound than control group. Moreover, it was also revealed suppressed IL-1β and TNF-α expression in diabetic mice after PES treatment, illustrating the decreased pro-inflammatory microenvironment, which is favorable for the diabetic wound healing. In addition, we also elucidated the potential molecular mechanism of PES promoting diabetic wound healing by proteomics analysis. The results showed that the promoted cell proliferation and migration ability may associate with the increased metabolism and cellular processes of transport and catabolism, cell motility through the mTOR signal pathway and the calcium ion influx. Furthermore, this photo-driven wireless electronic skin for refractory wound healing is cheap and easy to use, which not only provided an effective electrical stimulation pattern, but also provided a new therapeutic formula and theoretical basis for refractory wound healing. This work shows positive impact on the related wounds and defects healing such as dural defect, gastrointestinal injury and surgical wounds, and provided a physical and controllable strategy for refractory wound treatment.

Materials and methods

Fabrication of the micro-pillar p-type Si thin-film

The fabrication of micro-pillar p-type Si thin-film starts with silicon-on-insulator (SOI) wafers (top device layer 5 μm, boron doping concentration ~1.015×10^{9} m^{-3}, 0.01–0.10 Ω·m, (100) orientation, Soitec, France). The top Si device layers were firstly patterned into p-type micro-pillar arrays (pillars with ~2×10^{-6} m in height, ~1×10^{-6} m in diameter, and a period of 5×10^{-6} m) by photolithography (photoresist AZ5214, ~1.6×10^{-6} m 3000 rpm) and reactive-ion etching (RIE SF6 plasma, etching rate ~1.67×10^{-8} m/s). Secondly, the patterned mesh structures (hole size $3 \times 10^{-4} \times 3 \times 10^{-4}$ m^2, pitch 1×10^{-4} m) were fabricated via another photolithography (photoresist SPR 220, ~1.6×10^{-6} m, 3000 rpm) and dry-etching process respectively. Lastly, the free-standing p-type Si thin-film meshes are obtained by removing the silicon dioxide layer in a hydrofluoric acid solution. Poly (dimethylsiloxane) stamps pick up the released Si meshes and transfer them to target position.

Optoelectronic characterization of micro-pillar p-type Si thin-film

A standard patch-clamp setup was employed to measure the photon response performances of the p-type Si thin-films in PBS solution (pH 7.2–7.4, 0.79 g/L NaCl, 0.14 g/L Na_2HPO_4/NaH_2PO_4, and 0.019 g/L KCl). An 808 nm laser beam (~0.004 m spot size) was vertically incident on the surfaces of p-type Si thin-film and controlled by transistor-transistor logic signals for pulsed signals output. A pipette electrode (~3×10^{5} Ω) filled with PBS was placed close to (~3×10^{-6} m) the tested sample surface. The photocurrent signals were collected with the

voltage-clamp recording model with an Axopatch 200B amplifier controlled by pClamp software (Molecular Devices) under illumination (frequency, 10 Hz; pulse duration, 5 $\times 10^{-3}$ s).

Cell morphology

To investigate the adhesion of cells on micro-pillar p-type Si thin-film, the L929 cells were seeded on the micro-pillar p-type Si thin-film with the density of 5000 cells/well. The micro-pillar p-type Si thin-film was treated with dopamine hydrochloride for 2 h before seeding to promote the materials adhesiveness. DMEM with 10 % fetal bovine serum and 1 % penicillin-streptomycin was used for cell culture. After cultured for 24 h in cell incubator with a humidity atmosphere containing 5 % CO_2 at 37 °C, L929 cells were fixed by 4 % paraformaldehyde solution for 900 s at room temperature. Then L929 cells were incubated with FITC-phalloidin for 1800 s to stain the F-actins, and the nucleus were stained by DAPI solution for 300 s. After that, cell morphology was caught by confocal microscopy (Nikon A1, Japan).

Intracellular calcium ion level

24 h after L929 seeded on the micro-pillar p-type Si thin-film, intracellular calcium ion was dyed by Fluo-4 AM ester stock solution for 1800 s at 37 ℃, then the Fluo-4 AM ester stock solution was removed and washed by PBS solution for three times. The mother solution of Fluo-4 AM was 1.097 g/L, and it was diluted to 5.48 $\times$ 10^{-3} g/L before use. Then NIR irradiation (8.08 $\times 10^{-7}$ nm, 300 W/m^2) was applied on the L929 for various time, and the immunofluorescence image was acquired immediately after NIR irradiation by confocal microscopy. At the same time, the fluctuation of the average fluorescence intensity was recorded.

Transwell assay

The micro-pillar p-type Si thin-film was placed in the lower chamber of 24-well transwell, and L929 cells were seeded in the upper chamber with the density of 1 $\times$ 10^4 cells/mL. 1 mL cell suspension was added to the upper chamber of the transwell plate, and PES was applied for 600, 1200 and 1800 s. After that, the upper chamber and culture medium were removed. The L929 cells on micro-pillar p-type Si thin-film were washed and fixed by PBS and 4 % paraformaldehyde, respectively. Then the nucleus of L929 cells were stained by DAPI solution for 300 s. Afterwards, the quantity of cells was imaged and calculated by confocal microscopy and Image J software.

Cell proliferation

The proliferation of L929 cells with PES treatment was measured by cell counting kit-8 assay (CCK-8). Briefly, L929 cells were seeded in a 96-well plate with the density of 5000 cells/well, and PES was applied at 24 h after seeded, the CCK-8 assay was performed after another 24 h incubation. PES was applied 1200 s per day, after PES treated for 1, 2 and 3 d, 0.01 mL CCK-8 solution was added to the per well and incubated for 3 h in 5 % CO_2 at 37 ℃. The absorbance was read at 4.5 $\times$ 10^{-7} m to evaluate the cell proliferation by microplate reader.

Cell migration

The fibroblasts L929 was seeded on the micro-pillar p-type Si thin-film with the density of 5000 cells/well, and 24 h after seeding the PES was applied. L929 cells were treated for 600, 1200 and 1800 s per days, after PES treated for 3 d, the L929 was reached for cell confluence. Then a scratch was made by a 0.2 mL pipette tip on the monolayer of cells. The L929 cells were imaged by optical microscope at 0, 12, 24, 36 and 48 h after scratch. The wound closure ratio was calculated by the following formula: wound closure (%) = (A_0-A_i)/$A_0$$\times$ 100 %. Where A_0 represents the initial wound area, Ai represents the remaining wound area at 12, 24, 36 and 48 h.

Diabetic mice model establishment

Animal experiments were approved by the Animal Ethics Committee of Peking Union Medical College Hospital (XHDW-2020–036). Briefly, 6 weeks C57BL/6 male mice were purchased from Beijing Vital River Laboratory Animal Technology Co., Ltd, Beijing, China. All mice were housed in the cages for one week in an 12 h light/dark environment. Type 1 diabetic mice were induced by intraperitoneal injection of low dose STZ (4 $\times 10^{-5}$ g/g) for 5 d and high dose STZ (8 $\times 10^{-5}$ g/g) for 3 d, the mice were hunger for 4 h before injection and 10 % w/v was administrated within 12 h after STZ injection. Mice were regarded as diabetic when the blood glucose level was exceeded 2.5 g/L in two consecutive days after 5 d post injection. The blood glucose was recorded by a glucometer (Roche, Switzerland) through tail vein blood, and weight was measured by a weight scale.

Chitosan/β-sodium glycerophosphate hydrogel

Firstly, 0.5 g chitosan was dissolved in 10 mL 6 g/L acetic acid solution and stirred continuously until completely dissolved. β-sodium glycerophosphate was dissolved in ddH_2O with a final proportion of 80 % w/v. Then chitosan and β-sodium glycerophosphate were mixed with equal volume, with the final concentration of chitosan and β-sodium glycerophosphate were 2.5 % and 40 % w/v. This prepared hydrogel could solidify under 37 ℃ within 600 s, and it was not solidified at room temperature.

Skin wound and PES treatment

One week after the diabetic mice model established, the mice were anesthetized by intraperitoneal administration of 0.3 % pentobarbital sodium with the amount of 0.02 mL/g. Then a full thickness back skin wound with the diameter of 0.01 m was made, after that the micro-pillar p-type Si thin-film was placed onto the wound, and the prepared chitosan/β-sodium glycerophosphate hydrogel was injected and covered the wound to fix the p-type Si thin-film and avoid the microbial invasion. The wound mice were randomly divided into two treatment groups, one group was applied PES for 1200 s per day, and the other group given no stimulation. The PES treatment was continuous applied for 7 d. The wound area was recorded at 0, 7, 10, 14, 21 and 28 d after operations, and the wound closure area was calculated by the following formula: wound closure area (%) = (A_0-Ai)/A_0 $\times$ 100 %, where A_0 represents the initial wound area and Ai represents the wound area at different time points.

Histological and immunofluorescence evaluation

At 10, 14 and 28 d post-surgery, the wound and surrounding healthy skin tissues were collected and fixed by 4 % paraformaldehyde solution, dehydrated by a series of graded ethanol, and embedded in paraffin for histological and immunofluorescence analysis. 5 $\times$ 10^{-6} m thickness sections were prepared and stained with H&E. At the same time, the sections were blocked and incubated with primary antibody of IL-1β and TNF-α overnight at 4 ℃, then the sections were incubated with secondary antibody labelled with HRP for 3000 s at room temperature. At last, the sections were visualized by DAB developing and finally counterstained in nucleus with hematoxylin for 180 s. The expression level of IL-1β and TNF-α were counted using Image J software by choose three random fields.

Proteomics analysis

Label free Liquid Chromatography Mass Spectrometer (LC-MS) was used for proteomics analysis of diabatic mice skin tissue with and

without PES treatment after 2 weeks post surgery (n = 3). The proteins were extracted and digested firstly, then LC-MS was used to detect the peptides. The iProteome cloud platform was used for the MS data processing. Hierarchical clustering based on differentially expressed protein was visualized by a heat map. KEGG online tools and Pfam database were used for the KEGG and domain enrichment analysis. Protein-protein interaction was carried out by STRING interaction database (http:/string-db.org). A corrected $p < 0.05$ was considered significantly different.

CRediT authorship contribution statement

Zhao Yu: Writing – review & editing, Supervision, Funding acquisition. **Wang Hai:** Supervision, Conceptualization. **Wang Huachun:** Writing – original draft, Methodology, Investigation, Formal analysis, Data curation. **Li Jiahao:** Methodology, Data curation. **Wu Zhihong:** Supervision, Funding acquisition. **Tian Jingjing:** Writing – original draft, Visualization, Validation, Methodology, Investigation, Funding acquisition, Formal analysis, Data curation, Conceptualization. **Li Zhou:** Writing – review & editing, Supervision. **Yin Lan:** Project administration, Investigation. **Sheng Xing:** Supervision, Project administration, Methodology, Investigation, Conceptualization.

Declaration of Competing Interest

The authors declare that they have no known competing financial interests or personal relationships that could have appeared to influence the work reported in this paper.

Acknowledgment

This research was funded by Beijing Natural Science Foundation (L212010), National Natural Science Foundation of China (82272464, 62304264, 82172450), Fundamental Research Funds for the Central Universities (3332024113), CAMS Innovation Fund for Medical Sciences (CIFMS, 2022-I2M-2–001 to Z.W.)

Appendix A. Supporting information

Supplementary data associated with this article can be found in the online version at doi:10.1016/j.nantod.2025.102697.

Data availability

Data will be made available on request.

References

[1] S.R. Nussbaum, M.J. Carter, C.E. Fife, J. DaVanzo, R. Haught, M. Nusgart, D. Cartwright, Value Health 21 (2018) 27–32.
[2] Y. Cai, K. Chen, C. Liu, X. Qu, Bioact. Mater. 28 (2023) 243–254.
[3] R. Li, K. Liu, X. Huang, D. Li, J. Ding, B. Liu, X. Chen, Adv. Sci. 9 (2022) 2105152.
[4] Y. Kataoka, M. Kunimitsu, G. Nakagami, S. Koudounas, C.D. Weller, H. Sanada, Int. Wound J 18 (20212) 176-186.
[5] A.E. Campbell, A.R. McCready-Vangi, A. Uberoi, S.M. Murga-Garrido, V.M. Lovins, E.K. White, J.T.-C. Pan, S.A.B. Knight, A.R. Morgenstern, C. Bianco, P.J. Planet, S. E. Gardner, E.A. Grice, Cell Rep. 42 (2023) 113281.
[6] S. Matoori, A. Veves, D.J. Mooney, Sci Transl Med 13 (2021585) eabe4839.
[7] Y. Liang, J. He, B. Guo, ACS Nano 15 (2021) 12687–12722.
[8] J. Qu, X. Zhao, Y. Liang, Y. Xu, P.X. Ma, B. Guo, Chem. Eng. J. 362 (2019) 548–560.
[9] W. Lyu, Y. Ma, S. Chen, H. Li, P. Wang, Y. Chen, X. Feng, Adv. Health Mater. 10 (2021) 2100785.
[10] F.W. Brennfleck, C. Bongards, Int. Wound J. 20 (2023) 458–466.
[11] M. Rodrigues, N. Kosaric, C.A. Bonham, G.C. Gurtner, Physiol. Rev. 99 (2019) 665–706.
[12] R. An, Y. Zhang, Y. Qiao, L. Song, H. Wang, X. Dong, Stem Cell Res. Ther. 11 (2020) 120.
[13] M.A. Nieto, Ruby Y.-J. Huang, R.A. Jackson, J.P. Thiery, Cell 166 (2016) 21–45.
[14] R. Fan, C. Zhang, F. Li, B. Li, A. McCarthy, Y. Zhang, S. Chen, L. Zhang, Adv. Sci. 11 (2024) 2309993.
[15] Q. Huang, Y. Zeng, Y. Qiu, J. Zou, F. Li, X. Liu, A. Nezamzadeh-Ejhieh, H. Song, J. Liu, Dyes Pigments 222 (2024) 111865.
[16] L.-E. Deng, Y. Qiu, Y. Zeng, J. Zou, A. Kumar, Y. Pan, A. Nezamzadeh-Ejhieh, J. Liu, X. Liu, RSC Med. Chem. 15 (2024) 2601–2621.
[17] L. Wang, C. Lu, S. Yang, P. Sun, Y. Wang, Y. Guan, S. Liu, D. Cheng, H. Meng, Q. Wang, J. He, H. Hou, H. Li, W. Lu, Y. Zhao, J. Wang, Y. Zhu, Y. Li, D. Luo, T. Li, H. Chen, S. Wang, X. Sheng, W. Xiong, X. Wang, J. Peng, L. Yin, Sci. Adv. 6 (2020) eabc6686.
[18] L. Li, L. Lu, Y. Ren, G. Tang, Y. Zhao, X. Cai, Z. Shi, H. Ding, C. Liu, D. Cheng, Y. Xie, H. Wang, X. Fu, L. Yin, M. Luo, X. Sheng, Nat. Commun. 13 (2022) 839.
[19] H. Xu, Y. Huo, Q. Zhou, L.A. Wang, P. Cai, B. Doss, C. Huang, K.J. Hsia, Proc. Natl. Acad. Sci. 120 (2023) 2221040120.
[20] G.-H. Lee, H. Moon, H. Kim, G.H. Lee, W. Kwon, S. Yoo, D. Myung, S.H. Yun, Z. Bao, S.K. Hahn, Nat. Rev. Mater. 5 (2020) 149–165.
[21] I.S. Foulds, A.T. Barker, Br. J. Dermatol. 109 (1983) 515–522.
[22] R. Luo, Y. Liang, J. Yang, H. Feng, Y. Chen, X. Jiang, Z. Zhang, J. Liu, Y. Bai, J. Xue, S. Chao, Y. Xi, X. Liu, E. Wang, D. Luo, Z. Li, J. Zhang, Adv. Mater. 35 (2023) 2208395.
[23] L.E. Wolcott, P.C. Wheeler, H.M. Hardwicke, B.A. Rowley, South Med. J. 62 (1969) 795–801.
[24] L.C. Kloth, Nursing 32 (2002) 17.
[25] C. Wang, X. Jiang, H.-J. Kim, S. Zhang, X. Zhou, Y. Chen, H. Ling, Y. Xue, Z. Chen, M. Qu, L. Ren, J. Zhu, A. Libanori, Y. Zhu, H. Kang, S. Ahadian, M.R. Dokmeci, P. Servati, X. He, Z. Gu, W. Sun, A. Khademhosseini, Biomaterials 285 (2022) 121479.
[26] Y. Lu, Y. Wang, J. Zhang, X. Hu, Z. Yang, Y. Guo, Y. Wang, Acta Biomater. 89 (2019) 217–226.
[27] X. Huang, L. Wang, H. Wang, B. Zhang, X. Wang, R.Y.Z. Stening, X. Sheng, L. Yin, Small 16 (2020) 1902827.
[28] J. Tian, R. Shi, Z. Liu, H. Ouyang, M. Yu, C. Zhao, Y. Zou, D. Jiang, J. Zhang, Z. Li, Self-powered implantable electrical stimulator for osteoblasts' proliferation and differentiation, Nano Energy 59 (2019) 705–714.
[29] J. Tian, H. Feng, L. Yan, M. Yu, H. Ouyang, H. Li, W. Jiang, Y. Jin, G. Zhu, Z. Li, Nano Energy 36 (2017) 241–249.
[30] C. Tong, X. Zhong, Y. Yang, X. Liu, G. Zhong, C. Xiao, B. Liu, W. Wang, X. Yang, Biomaterials 243 (2020) 119936.
[31] A. Maleki, J. He, S. Bochani, V. Nosrati, M.-A. Shahbazi, B. Guo, ACS Nano 15 (2021) 18895–18930.
[32] J.H. Lee, Y. Ahn, H.E. Lee, Y.N. Jang, A.Y. Park, S. Kim, Y.H. Jung, S.H. Sung, J. H. Shin, S.H. Lee, S.H. Park, K.S. Kim, M.S. Jang, B.J. Kim, S.H. Oh, K.J. Lee, Adv. Health Mater. 12 (2022) 2201796.
[33] R. Luo, B. Shi, D. Luo, Z. Li, Sci. Bull. 68 (2023) 1740–1743.
[34] W. Tang, J. Tian, Q. Zheng, L. Yan, J. Wang, Z. Li, Z.L. Wang, ACS Nano 9 (2015) 7867–7873.
[35] J.H. Lee, S. Lee, D. Kim, K.J. Lee, Adv. Drug Deliv. Rev. 187 (2022) 114399.
[36] Y. Huang, Y. Cui, H. Deng, J. Wang, R. Hong, S. Hu, H. Hou, Y. Dong, H. Wang, J. Chen, L. Li, Y. Xie, P. Sun, X. Fu, L. Yin, W. Xiong, S.H. Shi, M. Luo, S. Wang, X. Li, X. Sheng, Nat. Biomed. Eng. 7 (2023) 486–498.
[37] J.F. Zimmerman, G.F. Murray, Y. Wang, J.M. Jumper, J.R. Austin, 2nd, B. Tian, Nano Lett. 15 (2015) 5492–5498.
[38] J.F. Zimmerman, R. Parameswaran, G. Murray, Y. Wang, M. Burke, B. Tian, Sci. Adv. 2 (2016) 1601039.
[39] Y. Jiang, X. Li, B. Liu, J. Yi, Y. Fang, F. Shi, X. Gao, E. Sudzilovsky, R. Parameswaran, K. Koehler, V. Nair, J. Yue, K. Guo, Y. Fang, H.-M. Tsai, G. Freyermuth, R.C.S. Wong, C.M. Kao, C.T. Chen, A.W. Nicholls, X. Wu, G.M. G. Shepherd, B. Tian, Nat. Biomed. Eng. 2 (2018) 508–521.
[40] D.R. Merrill, M. Bikson, J.G. Jefferys, J. Neurosci. Methods 141 (2005) 171–198.
[41] H. Wang, J. Tian, Y. Jiang, S. Liu, J. Zheng, N. Li, G. Wang, F. Dong, J. Chen, Y. Xie, Y. Huang, X. Cai, X. Wang, W. Xiong, H. Qi, L. Yin, Y. Wang, X. Sheng, Sci. Adv. 9 (2023) eabq7750.
[42] P. Sun, Y. Guan, C. Yang, H. Hou, S. Liu, B. Yang, X. Li, S. Chen, L. Wang, H. Wang, Y. Huang, X. Sheng, J. Peng, W. Xiong, Y. Wang, L. Yin, Adv. Health Mater. 12 (2023) 2301859.
[43] H. Wang, J. Tian, B. Lu, Y. Xie, P. Sun, L. Yin, Y. Wang, X. Sheng, Sensors 22 (2022) 802.
[44] H. Derikvandi, A. Nezamzadeh-Ejhieh, J. Hazard Mater. 321 (2017) 629–638.
[45] R. Fazaeli, H. Aliyan, A. Nezamzadeh-Ejhieh, D. Richeson, Surf. Interfaces 52 (2024) 104877.
[46] Y. Jiang, B. Tian, Nat. Rev. Mater. 3 (2018) 473–490.
[47] H. Kim, S. Beack, S. Han, M. Shin, T. Lee, Y. Park, K.S. Kim, A.K. Yetisen, S.H. Yun, W. Kwon, S.K. Hahn, Adv. Mater. 30 (2018) 1701460.
[48] X.M. Jiang, L.M. Wang, J. Wang, C.Y. Chen, Appl. Biochem. Biotechnol. 166 (2012) 1533–1551.
[49] Y. Liu, Y.L. Zhao, B.Y. Sun, C.Y. Chen, Acc. Chem. Res. 46 (2013) 702–713.
[50] A. Prominski, J. Shi, P. Li, J. Yue, Y. Lin, J. Park, B. Tian, M.Y. Rotenberg, Nat. Mater. 21 (2022) 647–655.
[51] N. Omrani, A. Nezamzadeh-Ejhieh, J. Mol. Liq. 315 (2020) 113701.
[52] F. Soleimani, A. Nezamzadeh-Ejhieh, J. Mater. Res. Technol. 9 (2020) 16237–16251.
[53] X. Liu, B. Gaihre, S. Park, L. Li, B. Dashtdar, M.D.A. Potes, A. Terzic, B.D. Elder, L. Lu, Bioact. Mater. 27 (2023) 216–230.
[54] Y. He, Y. Gao, Q. Ma, X. Zhang, Y. Zhang, W. Song, J. Nanobiotechnol. 20 (2022) 510.
[55] H.L. Sladitschek-Martens, A. Guarnieri, G. Brumana, F. Zanconato, G. Battilana, R. L. Xiccato, T. Panciera, M. Forcato, S. Bicciato, V. Guzzardo, M. Fassan, L. Ulliana,

A. Gandin, C. Tripodo, M. Foiani, G. Brusatin, M. Cordenonsi, S. Piccolo, Nature 607 (2022) 790–798.
[56] S. Zhang, B.J. Ma, F. Liu, J.Z. Duan, S.C. Wang, J.C. Qiu, D. Li, Y.H. Sang, C. Liu, D. Liu, H. Liu, Nano Lett. 18 (2018) 2243–2253.
[57] W. Heng, M. Bhavsar, Z. Han, J.H. Barker, Curr. Stem Cell Ther. 15 (2020) 441–448.
[58] M.T. Kucewicz, G.A. Worrell, N. Axmacher, Brain 146 (2023) 2214–2226.
[59] S. Monaco, M. Illario, M.R. Rusciano, G. Gragnaniello, G.D. Spigna, E. Leggiero, L. Pastore, G. Fenzi, G. Rossi, M. Vitale, Cell Cycle 8 (2009) 2024–2030.
[60] J. O'Hare, K.C. Gonzalez, S.A. Herrlinger, Y. Hirabayashi, V. Hewitt, H. Blockus, M. Szoboszlay, S.V. Rolotti, T.C. Geiller, A. Negrean, V. Chelur, F. Polleux, A. Losonczy, Science 375 (2022) eabm1670.
[61] A. Grada, M. Otero-Vinas, F. Prieto-Castrillo, Z. Obagi, V. Falanga, J. Invest Dermatol. 137 (2017) e11–e16.
[62] D. Li, L. Kular, M. Vij, E.K. Herter, X. Li, A. Wang, T. Chu, M.-A. Toma, L. Zhang, E. Liapi, A. Mota, L. Blomqvist, I.G. Sérézal, O. Rollman, J.D. Wikstrom, M. Bienko, D. Berglund, M. Ståhle, P. Sommar, M. Jagodic, N.X. Landén, Proc. Natl. Acad. Sci. 116 (2019) 9443–9452.
[63] O. Stojadinovic, I. Pastar, S. Vukelic, 784, M.G. Mahoney, D. Brennan, A. Krzyzanowska, M. Golinko, H. Brem, M. Tomic-Canic, J. Cell Mol. Med. 12 (2008) 2675–2690.
[64] W.J. Jeffcoate, L. Vileikyte, E.J. Boyko, D.G. Armstrong, A.J.M. Boulton, Diabetes Care 41 (2018) 645–652.
[65] G.C. Gurtner, S. Werner, Y. Barrandon, M.T. Longaker, Nature 453 (2008) 314–321.
[66] W. Hu, Q. Ouyang, C. Jiang, S. Huang, N.-E. Alireza, D. Guo, J. Liu, Y. Peng, Mater. Today Chem. 41 (2024) 102300.
[67] Y.J. Fu, Y.F. Shi, L.Y. Wang, Y.F. Zhao, R.K. Wang, K. Li, S.T. Zhang, X.J. Zha, W. Wang, X. Zhao, W. Yang, Adv. Sci. 10 (2023) 2206771.
[68] D. Baltzis, I. Eleftheriadou, A. Veves, Adv. Ther. 31 (2014) 817–836.
[69] F.M. Davis, A. Kimball, A. Boniakowski, K. Gallagher, Curr. Diab Rep. 18 (2018) 2.

Supplementary Materials

Photo-driven electronic skin enable activation of calcium channel for refractory wound healing

Jingjing Tian[a,c], Jiahao Li[b], Zhihong Wu[c,d,e,f], Lan Yin[g], Xing Sheng[h], Zhou Li[i], Hai Wang[b,*], Huachun Wang[j,*], Yu Zhao[b,k,l*]

a Biomedical Engineering Facility of National Infrastructures for Translational Medicine, Peking Union Medical College Hospital, Chinese Academy of Medical Sciences and Peking Union Medical College, Beijing, 100730, China

b Department of Orthopaedic Surgery, Peking Union Medical College Hospital, Chinese Academy of Medical Science and Peking Union Medical College, Beijing, 100730, China

c Medical Research Center, Peking Union Medical College Hospital, Chinese Academy of Medical Sciences and Peking Union Medical College, Beijing 100730, China

d State Key Laboratory of Complex Severe and Rare Diseases, Peking Union Medical College Hospital, Chinese Academy of Medical Sciences and Peking Union Medical College, Beijing 100730, China

e Beijing Key Laboratory for Genetic Research of Skeletal Deformity, Beijing 100730, China

f Key Laboratory of Big Data for Spinal Deformities, Chinese Academy of Medical Sciences, Beijing 100730, China

g The Key Laboratory of Advanced Materials of Ministry of Education, State Key Laboratory of New Ceramics and Fine Processing, School of Materials Science and Engineering, Tsinghua University, Beijing, 100084, China

h Department of Electronic Engineering, Beijing National Research Center for Information Science and Technology, Center for Flexible Electronics Technology, IDG/McGovern Institute for Brain Research, Tsinghua University, Beijing, 100084,

China

i Beijing Key Laboratory of Micro-nano Energy and Sensor, Beijing Institute of Nanoenergy and Nanosystems, Chinese Academy of Sciences, Beijing 101400, China

j School of Integrated Circuits, Shenzhen Campus of Sun Yat-sen University, Shenzhen, 518107, China

k State Key Laboratory of Common Mechanism Research for Major Diseases

l Institute of Basic Medical Sciences, Chinese Academy of Medical Sciences and Peking Union Medical College

* Correspondence author: zhaoyupumch@163.com (Y. Zhao); wanghch36@mail.sysu.edu.cn (H. C. Wang); wanghai907@hotmail.com (H. Wang)

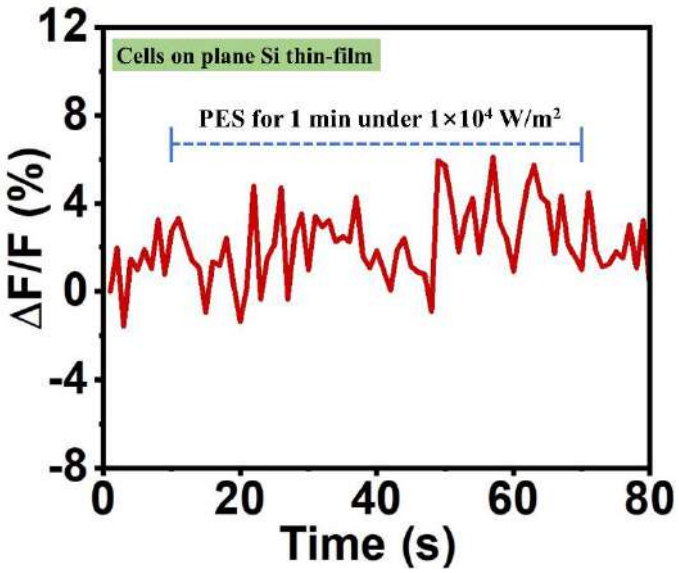

Figure S1 Intracellular calcium ion fluorescence intensity remains almost unchanged on plane Si thin-film under a higher illumination intensity of 1×10^4 W/m^2